Available online at www.sciencedirect.com
ScienceDirect
Trans. Nonferrous Met. Soc. China 31(2021) 2922−2938
Transactions of Nonferrous Metals Society of China
www.tnmsc.cn

Finite element analysis of temperature and stress fields during selective laser melting process of Al−Mg−Sc−Zr alloy

Ru-long MA[1], Chao-qun PENG[1], Zhi-yong CAI[1,2], Ri-chu WANG[1,2], Zhao-hui ZHOU[3], Xiao-geng LI[3], Xuan-yang CAO[3]

1. School of Materials Science and Engineering, Central South University, Changsha 410083, China;
2. National Key Laboratory of Science and Technology on High-strength Structural Materials, Central South University, Changsha 410083, China;
3. Changsha Advanced Materials Industrial Research Institute, Changsha 410083, China

Received 14 October 2020; accepted 5 April 2021

Abstract: A 3D finite element model was established to investigate the temperature and stress fields during the selective laser melting process of Al−Mg−Sc−Zr alloy. By considering the powder−solid transformation, temperature-dependent thermal properties, latent heat of phase transformations and molten pool convection, the effects of laser power, point distance and hatch spacing on the temperature distribution, molten pool dimensions and residual stress distribution were investigated. Then, the effects of laser power, point distance and hatch spacing on the microstructure, density and hardness of the alloy were studied by the experimental method. The results show that the molten pool size gradually increases as the laser power increases and the point distance and hatch spacing decrease. The residual stress mainly concentrates in the middle of the first scanning track and the beginning and end of each scanning track. Experimental results demonstrate the accuracy of the model. The density of the samples tends to increase and then decrease with increasing laser power and decreasing point distance and hatch spacing. The optimum process parameters are laser power of 325−375 W, point distance of 80−100 μm and hatch spacing of 80 μm.

Key words: aluminum−magnesium alloy; Al−Mg−Sc−Zr alloy; selective laser melting; finite element analysis; temperature field; stress field

1 Introduction

Selective laser melting (SLM), one of the three-dimensional (3D) printing technologies, has been extensively used in the fabrication of Ti-based alloys [1−3], Fe-based alloys [4,5], and Al alloys [6−9] due to obvious advantages such as low tooling cost, short design and production period, and unlimited design freedom, especially for the complex shape components. So far, selective laser melted Al−Mg alloys have attracted extensive interest of many researchers owing to their high strength, excellent corrosion resistance, and good weldability. SPIERINGS et al [10,11] reported that the tensile strength of the selective laser melted Al−Mg−Sc−Zr alloy reaches 530 MPa because of the precipitation of Al_3(Sc,Zr) particles and fine grain structure of the alloy. ZHANG et al [12] studied the evolution of Al_3(Sc,Zr) particles of the selective laser melted Al−Mg−Sc−Zr alloy under different scanning speeds and reported that some spherical Al_3(Sc,Zr) particles were mainly embedded at the bottom of the molten pool at a low scanning speed. MA et al [13] studied the effect of heat treatment on the microstructure and precipitates evolutions of selective laser melted Al−Mg−Sc−Zr alloy and found that the bimodal

Corresponding author: Zhi-yong CAI, Tel: +86-731-88836638, E-mail: zycaimse@163.com
DOI: 10.1016/S1003-6326(21)65703-5

microstructure and grain size of the alloy do not change significantly during the heat treatment process due to the Al_3(Sc,Zr) and Al_6Mn particles along the grain boundaries preventing grain growth.

In the selective laser melting process, the metal powders are melted and solidified instantaneously, and the cooling rate reaches 10^3−10^8 °C/s [14]. Such a high cooling rate leads to a high thermal stress, resulting in the occurrence of defects such as cracks, warpage and deformation. These defects are detrimental to the microstructure and mechanical properties of the alloy. In essence, these defects are related to the evolution of the temperature and stress fields in the molten pool during the selective laser melting process. Thus, it is important to study the evolution of temperature and stress fields, which, in turn, helps to optimize the processing parameters. In addition, a combination of numerical simulation and experiment will greatly improve the efficiency of process parameter optimization and become an important trend in the future for the additive manufacturing industry.

Many numerical calculation models have been proposed to study the powder spreading, temperature, stress and flow fields in the selective laser melting process. CHEN et al [15,16] investigated the packing quality of powder layer in additive manufacturing by experiments and numerical simulations. ILIN et al [17] studied the effect of laser power and scanning speed on 316L stainless steel fabricated by selective laser melting using a 2D finite element model, and found that the simulation results were basically consistent with the experimental data. Excessively low scanning speed will lead to an unstable molten pool size. WEINGARTEN et al [18] analyzed the quasi-stationary temperature field for a single track of selective laser melted AlSi10Mg alloy, and found that the laser spot diameter had the greatest effect on the maximum temperature of the molten pool. However, current simulation research on Al alloys is mainly focused on Al−Si alloys, and there are few literatures on the 3D finite element simulation of selective laser melted Al−Mg alloys. In addition, the effects of thermal properties of the materials varying with temperature on the temperature field are not considered in most of the finite element models. Therefore, it is necessary to study the finite element simulation of selective laser melted Al−Mg alloy.

In this work, a 3D finite element model was established using the ANSYS APDL software program to simulate the temperature and stress fields during the selective laser melting process of Al−4.0Mg−0.7Sc−0.4Zr−0.5Mn (Al−Mg−Sc−Zr) alloy. The powder−solid transformation, temperature-dependent thermal properties, latent heat of phase transformations and molten pool convection were taken into account. Based on the model, the effects of laser power, point distance and hatch spacing on the temperature distribution, molten pool size, overlapping rate and residual stress distribution were investigated. Furthermore, corresponding experiments were performed to confirm the reliability of the simulation results and optimize the process parameters.

2 Finite element theories and model descriptions

The selective laser melting process contains a variety of physical phenomena, such as the interaction between the laser and the powders, the phase transformation, and the thermal conduction, convection and radiation. In order to simplify the model and improve the calculation efficiency, some factors in the finite element model need to be simplified.

2.1 Finite element model

The 3D finite element model for three layers and five tracks was developed for the temperature fields simulation in ANSYS APDL 19.0. The schematic simulation model and laser scanning strategy are shown in Fig. 1. By considering the accuracy and efficiency of simulation and referring to the literatures [19,20], the finite element model consists of 6061 substrate and Al−Mg−Sc−Zr powder bed with dimensions of 1.2 mm × 0.72 mm × 0.2 mm and 1.0 mm × 0.52 mm × 0.09 mm, respectively. The powder layer thickness is 30 μm. The moving direction of the laser beam is along the *x*-axis and the building direction is along the *z*-axis. The hexahedral SOLID 70 element and mapping method were used to mesh the model. Considering the accuracy and efficiency of the numerical simulation, a 0.01 mm × 0.01 mm × 0.01 mm mesh and a relatively large mesh were applied to the powder bed and the substrate, respectively. The

total number of meshes in the model is 95024, and the total number of nodes is 99447. Considering the computational efficiency, a mode for one layer and five tracks was used in the stress fields simulation. The dimension of powder bed was changed to 1.0 mm × 0.52 mm × 0.03 mm. The total number of meshes and nodes in the model are 74224 and 78035, respectively.

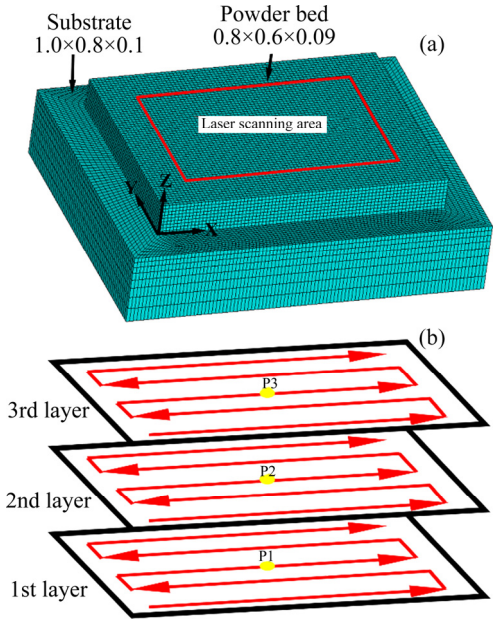

Fig. 1 Finite element model (a) and laser scanning strategy diagram (b) (Unit: mm)

2.2 Thermal modelling

2.2.1 Governing equations of heat transfer

The moving laser beam is used as the heat source in selective laser melting, and the temperature of powder bed changes with the laser spot moving. Therefore, selective laser melting is a typical nonlinear transient heat conduction process. According to the law of conservation of energy, the heat conduction equation is as follows [21,22]:

$$\rho c\frac{\partial T}{\partial t}=\frac{\partial}{\partial x}(k_x\frac{\partial T}{\partial x})+\frac{\partial}{\partial y}(k_y\frac{\partial T}{\partial y})+\frac{\partial}{\partial z}(k_z\frac{\partial T}{\partial z})+Q \tag{1}$$

where T is the temperature; k is the thermal conductivity; x, y, and z are the coordinates; Q is the unit volume heat generated per volume within the powder bed; ρ is the powder density; c is the specific heat capacity; t is the time.

Before the selective laser melting process (t=0), the temperatures of the powder bed, substrate and environment are defined as

$$T(x,y,z,t)|_{t=0}=T_0(x,y,z\in\mathbf{R}) \tag{2}$$

where T_0 is taken as 25 °C.

In the selective laser melting process, the molten pool is produced by pulsing heat of the moving laser beam. The heat within the molten pool is mainly lost by thermal convection and radiation, which are regarded as boundary conditions in the finite element model.

The thermal convection between the outer surface of the finite element model and the environment is defined as [20]

$$-\lambda_e\frac{\partial T}{\partial \boldsymbol{n}}=h(T-T_m) \tag{3}$$

where λ_e is the effective thermal conductivity of the powder; $\boldsymbol{n}$ is the vector along the normal direction of the top of the powder bed; h is the convective heat transfer coefficient; T_m is the environment temperature.

The thermal radiation is defined as [20]

$$-\lambda_e\frac{\partial T}{\partial \boldsymbol{n}}=\sigma_{SB}\epsilon(T^2+T_m^2)(T+T_m)(T-T_m)=\beta_0(T-T_m) \tag{4}$$

where σ_{SB} is the Stefan−Boltzman constant taken as 5.67×10^{-8} W/(m^2·K^4), ϵ is the emissivity of the material, and β_0 is the radiative heat transfer coefficient. Considering the convective heat transfer and radiation heat transfer comprehensively, the two heat transfer boundary conditions can be defined as [20]

$$-\lambda_e\frac{\partial T}{\partial \boldsymbol{n}}=\beta(T-T_m) \tag{5}$$

where β is the equivalent heat transfer coefficient.

2.2.2 Gaussian heat source modelling

The Nd:YAG fiber laser, which has high laser energy density and strong penetrability, was used in the selective laser melting process. The laser energy was loaded on the top surface of the powder bed in the form of heat flux. The laser energy density approximately meets the Gaussian distribution. The Gaussian heat source (q) can be defined as [19]

$$q=\frac{2AP}{\pi R_L^2}\exp(-\frac{2r^2}{R_L^2}) \tag{6}$$

where A is the laser absorptivity of the powder; P is the laser power; R_L is the laser spot radius; r is the radial distance between the node (x, y) and the laser spot center. Based on the reports of BEIRANVAND et al [23], A is taken as 0.18 in this work.

2.2.3 Thermophysical properties of materials

The model includes three materials: Al−Mg−Sc−Zr powder, Al−Mg−Sc−Zr solid and 6061 alloy substrate. The densities, thermal conductivities, and specific heats of the solid and substrate at different temperatures were calculated using JMatPro software. When the temperature exceeds the melting point of the powder (635 °C), the heat conduction will be accelerated due to the Marangoni convection within the molten pool, so the thermal conductivity coefficients were introduced in the simulation, and the thermal conductivities of the liquid are defined as

$$k_{xl} = w_x k_x,\ k_{yl} = w_y k_y,\ k_{zl} = w_z k_z \tag{7}$$

where k_{xl}, k_{yl} and k_{zl} are the thermal conductivities of the liquid, respectively; w_x, w_y and w_z are the thermal conductivity coefficients in x, y and z direction, respectively. In this work, the thermal conductivity coefficients are set to be ω_x=4, ω_y=4, and ω_x=5, respectively.

The density of the powder is given as [19]

$$\rho_p = \phi\rho_g + (1-\phi)\rho_s \tag{8}$$

where ρ_p, ρ_s and ρ_g are the densities of powder, solid and argon shielding gas, respectively, and ϕ is the porosity of the powder bed and it is defined as [24]

$$\phi = \frac{\rho_s - \rho_p}{\rho_s} \tag{9}$$

here, ρ_s and ρ_p are set to be 1.420 and 2.658 g/cm^3, respectively.

The thermal conductivity of the powder is given as [24]

$$k_p = k_s(1-\phi) \tag{10}$$

where k_p and k_s are the thermal conductivities of powder and solid, respectively.

In the selective laser melting process, the phase transformation process of the alloy will absorb or release heat, which is called latent heat of phase transformations. The latent heat of phase transformations has an important influence on the numerical simulation of the temperature field. Generally, the latent heat of phase transformations is expressed in the form of enthalpy H, which is defined as [19]

$$H = \int_{T_0}^{T} \rho c_p \mathrm{d}T \tag{11}$$

where c_p is the specific heat capacity.

The temperature-dependent thermophysical properties of powder, solid and substrate are illustrated in Fig. 2.

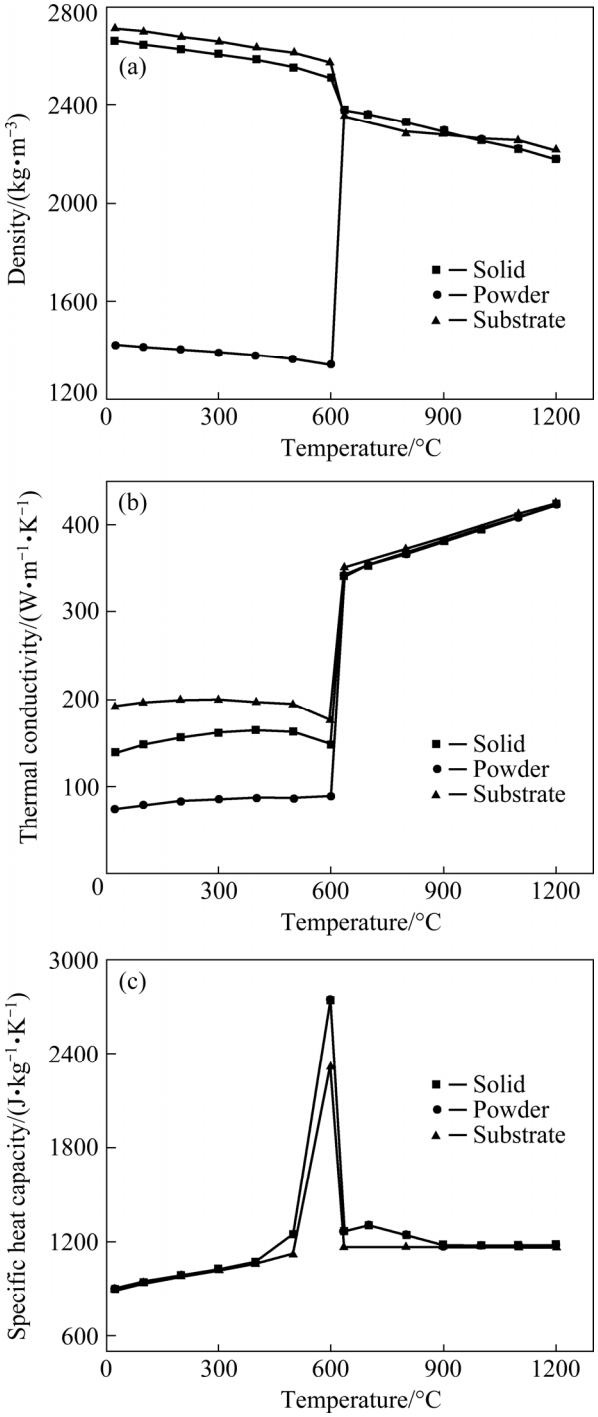

Fig. 2 Density (a), thermal conductivity (b) and specific heat capacity (c) of materials

The simulation cases under different laser powers, hatch spacings and point distances are listed in Table 1. Hatch spacing refers to the distance between two adjacent scanning tracks, and point distance refers to the distance of two adjacent

laser spots on the same scanning track [20]. The range of laser power is 200−400 W when the hatch spacing and point distance are fixed at 80 and 80 μm, respectively. The range of hatch spacing is 40−120 μm when the laser power and point distance are fixed at 350 W and 80 μm, respectively. The range of point distance is 30−130 μm when the laser power and hatch spacing are fixed at 350 W and 80 μm, respectively. The time step in the simulation is 2 μs.

Table 1 Process parameters used in simulation

Parameter	Value
Laser power, P/W	200, 250, 300, 350, 400
Hatch spacing, S/μm	40, 60, 80, 100, 120
Point distance, F/μm	30, 55, 80, 105, 130
Laser diameter, D/μm	70
Laying powder time, t_L/s	10
Exposure time, t_E/μs	60
Powder layer thickness, d/μm	30

2.2.4 Birth and death technology

In the finite element simulation process, the model of three layers and five tracks is established once in the modeling stage. However, 3D solid parts are prepared by a layer-by-layer method in the actual selective laser melting process. To solve this problem, birth and death technology [20] was used in the simulation. During the calculation of the first layer, all the elements of the subsequent processing layers (that is, the second and third layer) are "killed" to ensure that the temperature field simulation results of the first layer will not affect the subsequent processing layer. When the simulation calculation of the first layer is completed, the second layer is reactivated for calculation. This procedure is repeated until all the calculation has been completed.

2.3 Stress analysis

2.3.1 Governing equations of stress analysis

For isotropic materials, the relationship between stress and strain follows the thermal elastic−plastic theory and can be defined in Cartesian coordinates as [25]

$$\varepsilon_x = \frac{1}{E}\left[\sigma_x \nu(\sigma_y + \sigma_z) + \alpha\Delta T\right] \tag{12}$$

$$\varepsilon_y = \frac{1}{E}\left[\sigma_y \nu(\sigma_x + \sigma_z) + \alpha\Delta T\right] \tag{13}$$

$$\varepsilon_z = \frac{1}{E}\left[\sigma_z \nu(\sigma_x + \sigma_y) + \alpha\Delta T\right] \tag{14}$$

where E is the elastic modulus, ν is the Poisson's ratio, and α is the thermal expansion coefficient.

The initial stress σ at t=0 s is defined as

$$\sigma|_{t=0} = 0 \tag{15}$$

During the simulation of the stress field, displacement constraints in different directions were imposed at the substrate, which are defined as

$$\frac{\partial^2 u}{\partial t^2}|_{z_0} = 0,\ u|_{z_0} = 0 \tag{16}$$

$$\frac{\partial^2 v}{\partial t^2}|_{z_0} = 0,\ v|_{z_0} = 0 \tag{17}$$

$$\frac{\partial^2 w}{\partial t^2}|_{z_0} = 0,\ w|_{z_0} = 0 \tag{18}$$

where z_0 represents the substrate.

The Von Mises yield criterion was used in this model. The equivalent stress, which is also known as Von Mises stress, is used to evaluate the residual stress, and is defined as [20]

$$\bar{\sigma} = \frac{\sqrt{2}}{2}\sqrt{(\sigma_1 - \sigma_2)^2 + (\sigma_2 - \sigma_3)^2 + (\sigma_3 - \sigma_1)^2} \tag{19}$$

where σ_1, σ_2 and σ_3 are the first, second and third principal stresses, respectively.

2.3.2 Material properties analysis

The elastic modulus, Poisson's ratio and thermal expansion coefficient were calculated using JMatPro software. The yield strength and plastic tangent modulus were measured using a tensile test. The temperature-dependent material properties in the stress analysis are listed in Table 2.

Table 2 Mechanical properties of Al−Mg−Sc−Zr alloy at different temperatures

Temperature/ °C	Elastic modulus/ GPa	Yield strength/ MPa	Poisson's ratio	Thermal expansion coefficient/ (10^{-6} °C^{-1})
25	74.8	360	0.33	20.3
100	72.4	270	0.34	21.2
200	68.8	220	0.35	22.1
300	54.4	170	0.36	22.9
400	43.3	100	0.37	23.0

3 Experimental

The powder with a nominal composition of Al−4.0Mg−0.7Sc−0.4Zr−0.5Mn was prepared for selective laser melting. Details on the powder properties were reported in Ref. [26]. Based on the simulation results, the narrowed process parameters used in the experiment are listed in Table 3. The range of laser power is 300−400 W when the hatch spacing and point distance are fixed at 80 and 80 μm, respectively. The range of hatch spacing is 60−100 μm when the laser power and point distance are fixed at 350 W and 80 μm, respectively. The range of point distance is 40−120 μm when the laser power and hatch spacing are fixed at 350 W and 80 μm, respectively. Other process parameters are consistent with the finite element simulation. The samples with dimensions of 10 mm × 10 mm × 10 mm were fabricated by a Renishaw AM400 instrument. The selective laser melting process was performed under an Ar atmosphere with less than 0.1% oxygen content.

Table 3 Process parameters used in experiment

Parameter	Value
Lase power, *P*/W	300, 325, 350, 375, 400
Hatch spacing, *S*/μm	60, 70, 80, 90, 100
Point distance, *F*/μm	40, 60, 80, 100, 120

The samples were ground with SiC sand paper, polished with 0.5 μm diamond suspension and etched using Keller's reagent. The microstructure was then observed using optical microscopy (OM, MA100L, Nikon) and field emission scanning electron microscopy (SEM, SIRION200, FEI). The density of the samples was measured by the Archimedes method. The hardness was measured with a Shimadzu HMV−2T microhardness meter.

4 Results and discussion

4.1 Temperature field simulation

4.1.1 Temperature field distribution characteristics

In the selective laser melting process, the temperature distribution of the powder bed changes rapidly with the high-speed movement of the laser beam. The simulation results under laser power 350 W, point distance 80 μm, and hatch spacing 80 μm are taken as the example to study the temperature field. Figure 3 shows the top and cross-sectional views of the simulated transient temperature distribution as the laser beam moves to P1, P2 and P3 (the middle of the third scanning track of the first, second and third layer, respectively), respectively. The black dashed line indicates the liquidus of the Al−Mg−Sc−Zr alloy, and the region surrounded by the black dashed line represents the molten pool. As can be seen, the shape of the molten pool is comet tail profile. Compared with the rear side, the distribution of isotherms on the forepart side of the molten pool is denser, indicating a higher temperature gradient. This phenomenon is attributed to the higher thermal conductivity of the formed solid than that of the powder. When the laser beam moves from P1 to P2, the width and depth of the molten pool decrease from 132 to 125 μm and from 60 to 59 μm, respectively. The reason for the decrease in molten pool size is caused by the lower thermal conductivity of the melted powder than that of the substrate. When the laser beam continues to move to P3, the width and depth of the molten pool are 125 and 59 μm, respectively. Compared with P2 in the second layer, the molten pool size at P3 is basically stabilized. The calculation results show that the length of the molten pool (134−146 μm) is larger than the point distance (80 μm), the width of the molten pool (125−132 μm) is larger than the hatch spacing (80 μm), and the depth of the molten pool (59−60 μm) is larger than the powder layer thickness (30 μm). Therefore, the adjacent molten pool overlaps each other, which ensures a good metallurgical bonding in the alloy.

The overlapping rate has an important effect on selective laser melting characteristics such as surface quality and forming defects [27]. When the overlapping rate is too low, there will be obvious depression between the adjacent molten pools, resulting in poor surface roughness of the alloy, and the unmelted powder in the discontinuity zone can lead to defects such as pores and cracks; when the overlapping rate is too high, the overlapping area is elevated, which is detrimental to the forming process. The overlapping rate between the adjacent tracks, denoted by *R*, is expressed as

$$R=\frac{W-S}{W}\times 100\% \tag{20}$$

where W is the molten pool width.

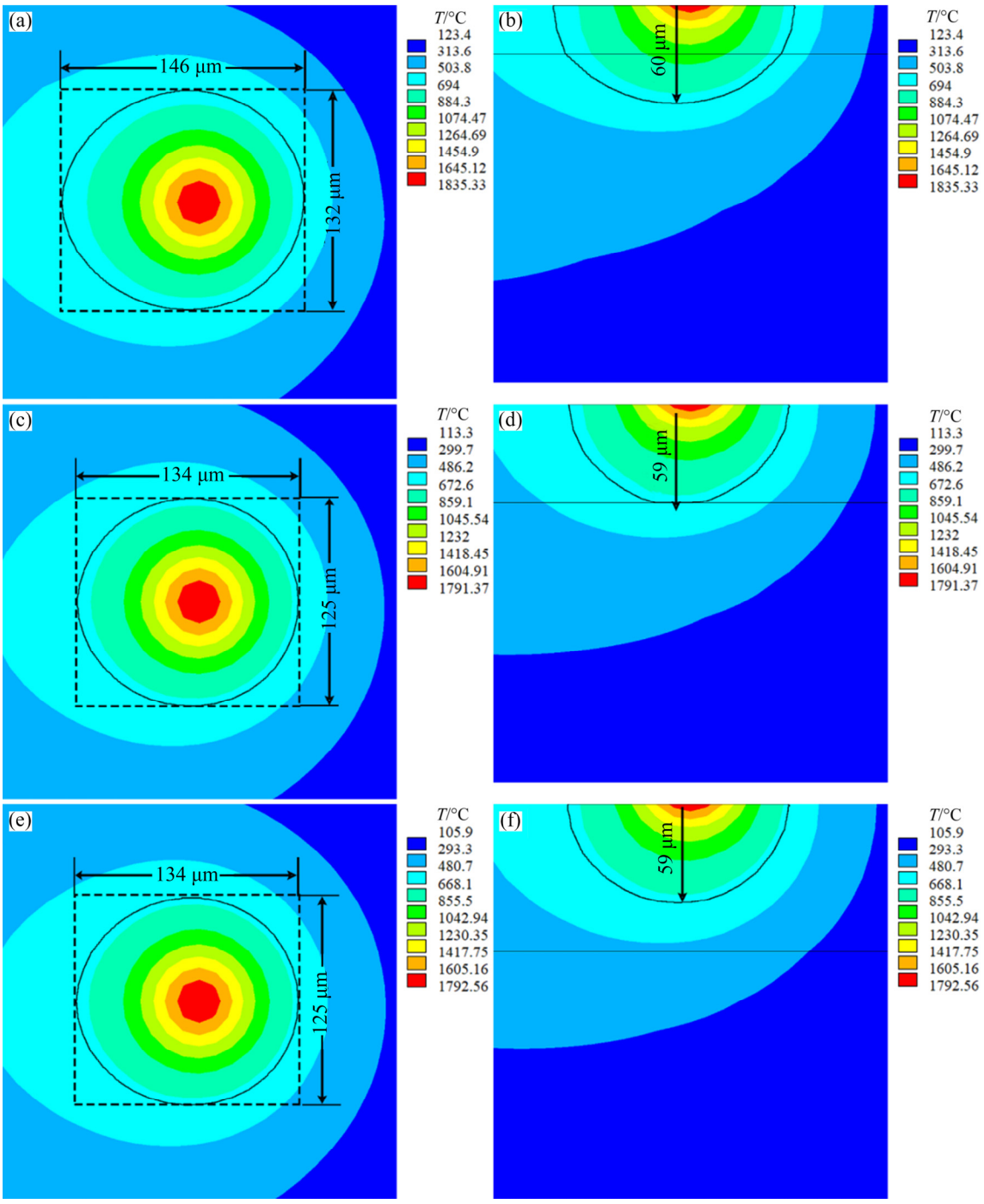

Fig. 3 Top (a, c, e) and cross-sectional (b, d, f) views of molten pool temperature fields under laser power of 350 W, point distance of 80 μm, and hatch spacing of 80 μm with laser moving to P1 (a, b), P2 (c, d), and P3 (e, f) (P1, P2 and P3 are located in the middle of the third scanning track of the first, second and third layers, respectively)

For pulse laser selective melting, it is also necessary to study the overlapping rate between the adjacent molten pools (R') in a single scanning track, which is expressed as

$$R' = \frac{L - F}{L} \times 100\% \tag{21}$$

where L is the molten pool length.

According to the Refs. [28,29], when the overlapping rate is 30%−50%, good metallurgical bonding can ensure better forming quality. The overlapping rates R and R' at P1, P2 and P3 are calculated to be 39.4%, 36.0%, 36.0% and 45.2%, 40.3%, 40.3%, respectively, which meet the overlapping rate requirements for aluminum alloys.

Figure 4 shows the transient temperature and cooling rate curves as a function of time at P1, P2, and P3. The dotted line represents the melting point of the alloy. As can be seen, there are generally five obvious peaks in each wavy curve during each layer scanning process, where each peak represents a laser scanning. As the laser beam approaches and moves away, the temperature rapidly increases and then rapidly decreases. As shown in Fig. 4(a), the maximum temperatures at P1, P2 and P3 are 1835.3, 1791.4 and 1792.6 °C, respectively. It can be seen that as the scanning layer increases, the temperature field becomes basically stable. When the laser moves to P2, the temperature at P1 increases above the melting point, indicating the remelting of the alloy at P1. Since two molten pools at P1 and P2 overlap, a good metallurgical bonding between the adjacent layers is ensured. The cooling rates at P1, P2, and P3 near the melting point are calculated to be 1.2×10^6, 2.3×10^6, and 2.6×10^6 °C/s, respectively (see Fig. 4(b)). The cooling rate of selective laser melting is much higher than that of the cast, which is helpful for the preparation of fine grain alloys.

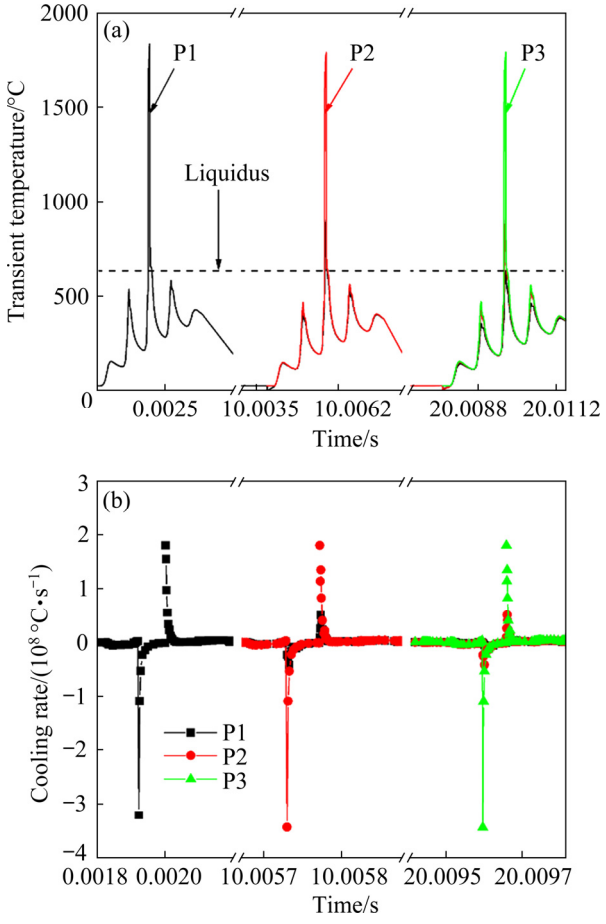

Fig. 4 Transient temperature (a) and cooling rate (b) versus time at P1, P2, and P3 in model

What's more, such a high cooling rate is also conducive to the solid solution of alloying elements such as Mg in the Al matrix to obtain high-performance alloy.

4.1.2 Thermal behavior with different process parameters

Process parameters have an important effect on the temperature field. The appropriate process parameters can effectively avoid the defects and improve the quality of the alloy parts. Therefore, it is necessary to study the effect of process parameters on the temperature field.

Figure 5 shows the effects of laser power on the temperature−time curve, maximum temperature, cooling rate, molten pool size and overlapping rate at P2 (the middle of the third scanning track of the second layer) with point distance 80 μm and hatch spacing 80 μm. As the laser power increases from 200 to 400 W, the maximum temperature and liquid lifetime increase sharply from 1221.5 to 1981.8 °C and from 70 to 133 μs, respectively. Relatively longer liquid lifetime is helpful for a larger molten pool. However, excessive temperature and liquid lifetime can result in strong thermal agitation and decrease liquid viscosity, leading to instability of the liquid in the molten pool. Thus, the liquid is easier to spatter from the molten pool, which is detrimental to the forming quality. Additionally, the cooling rate near the melting point decreases from 10.1×10^6 to 1.13×10^6 °C/s with the increase of laser power. The molten pool size and overlapping rate increase almost linearly as the laser power increases (see Fig. 5(c, d)). When the laser power increases from 200 to 400 W, the width of the molten pool increases from 89 to 135 μm, the depth increases from 34 to 64 μm, and the overlapping rate R and R' increase from 10.1% to 40.7% and from 10.1% and 46.3%, respectively. LI and GU [30] studied the effect of laser power on the selective laser melted AlSi10Mg and also found the same results. The overlapping rate at the laser power of 200 and 250 W is actually lower than 30%. This degrades the quality of the formed layer due to poor metallurgical bonding between adjacent scanning tracks. Therefore, the laser power should be 300−400 W to ensure better forming quality.

Figure 6 shows the effects of point distance on the temperature−time curve, maximum temperature, cooling rate, molten pool size and overlapping rate at P2 with laser power 350 W and hatch spacing 80 μm. When the point distance increases from 30

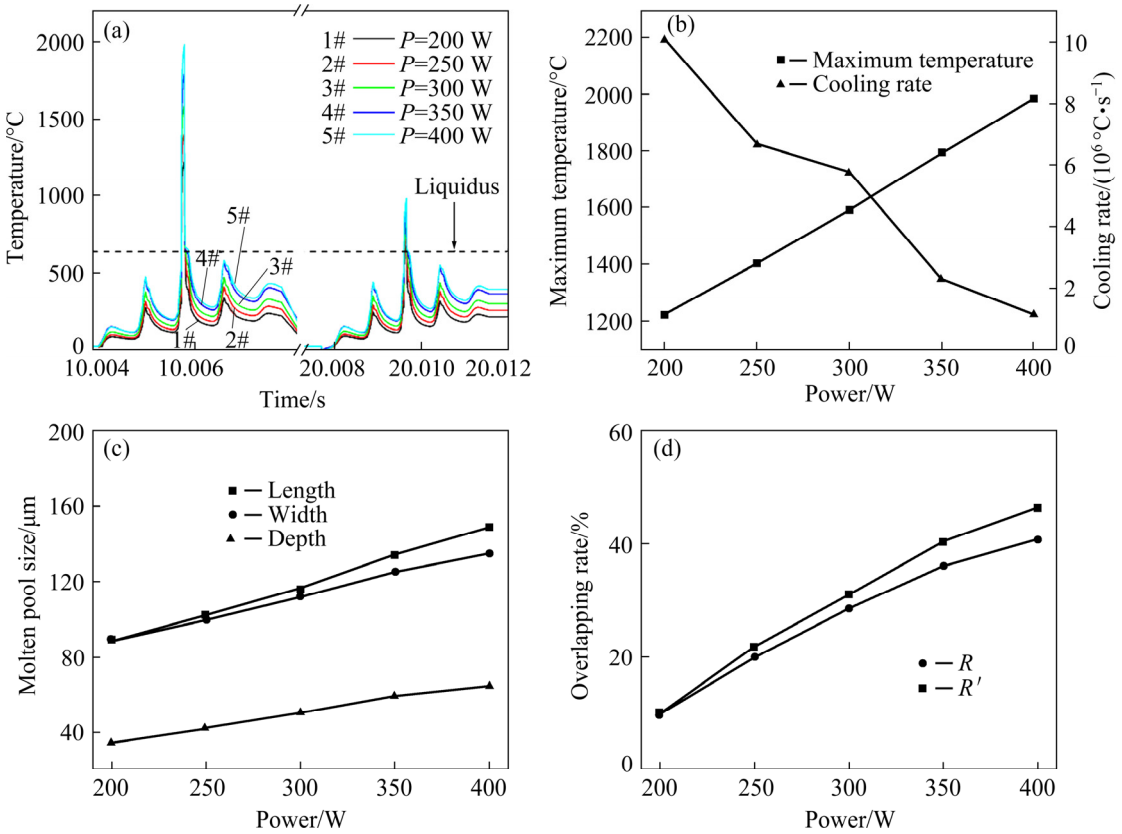

Fig. 5 Temperature−time curves (a), maximum temperature and cooling rate (b), molten pool size (c), and overlapping rate (d) at P2 under different laser powers with point distance of 80 μm and hatch spacing of 80 μm

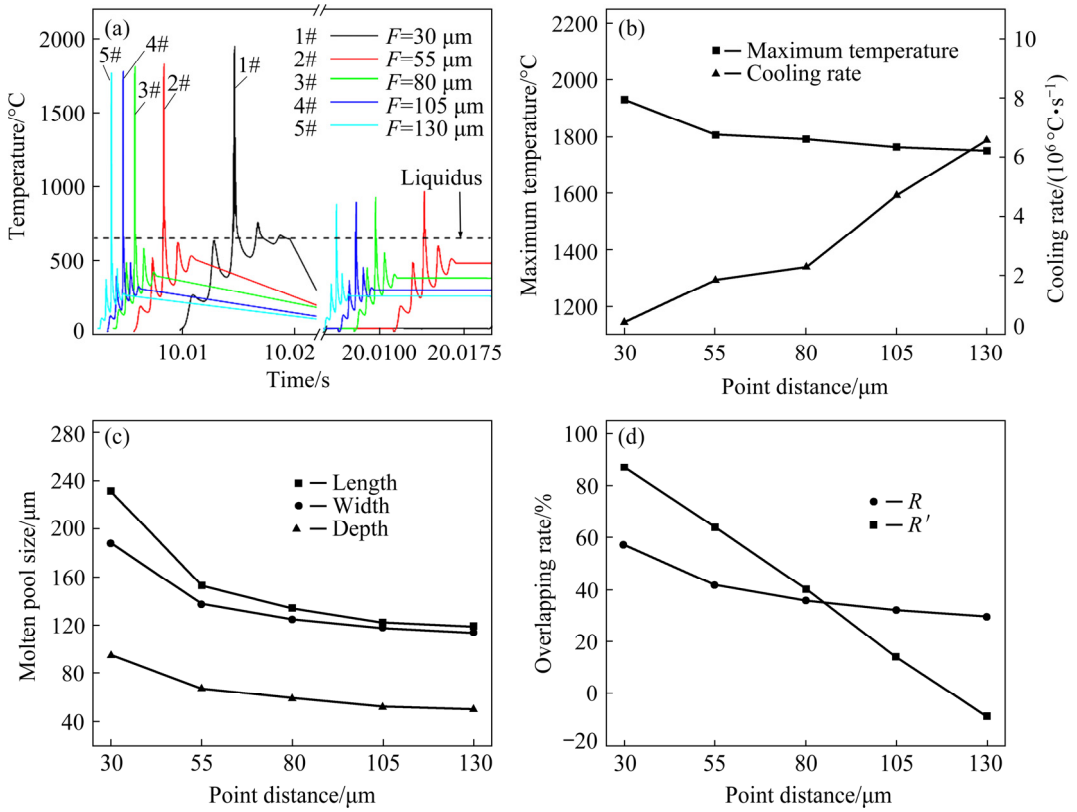

Fig. 6 Temperature−time curves (a), maximum temperature and cooling rate (b), molten pool size (c), and overlapping rate (d) at P2 with different point distances under laser power of 350 W and hatch spacing of 80 μm

to 130 μm, the maximum temperature decreases from 1931.7 to 1749.9 °C, and the cooling rate increases from 0.43×10^6 to 6.58×10^6 °C/s. At the same time, the molten pool size and overlapping rate gradually decrease as the point distance increases. As the point distance increases, the laser energy density decreases, resulting in a decrease in molten pool size. When the point distance is 130 μm, the overlapping rate R' is negative (−9.2%), indicating that some powders are unmelted and there is no metallurgical bonding between adjacent molten pools, which will lead to failure of the alloy forming. Considering the cooling rate and overlapping rate, the optimal point distance is 80 μm.

Figure 7 shows the effects of hatch spacing on the temperature−time curve, maximum temperature, cooling rate, molten pool size and overlapping rate at P2 with laser power 350 W and point distance 80 μm. As can be seen, as the hatch spacing increases from 40 to 120 μm, the maximum temperature gradually decreases from 1790.2 to 1782.2 °C, and the length, width, and depth of molten pool decrease slightly from 133, 125 and 60 μm to 130, 123 and 58 μm, respectively. The results show that the hatch spacing has little effect on the maximum temperature and molten pool size. This is because that the hatch spacing does not affect the laser energy input and laser action time of each individual molten pool. However, the hatch spacing has a great effect on the overlapping rate R. The overlapping rate R decreases sharply from 68% to 2.4% with the increasing hatch spacing. According to Eq. (20), the overlapping rate R is inversely proportional to the hatch spacing. Therefore, in the case of small changes in the molten pool size, the overlapping rate R decreases sharply as the hatch spacing increases. Considering the cooling rate and overlapping rate, the optimal hatch spacing ranges from 60 to 100 μm to ensure good forming quality.

4.2 Stress field simulation

4.2.1 Thermal stress evolution and residual stress distribution

During the selective laser melting process, the stress field of the powder bed is constantly changing due to the constant movement of the laser. In order to study the evolution of thermal stress in the powder bed, the stress fields at different time

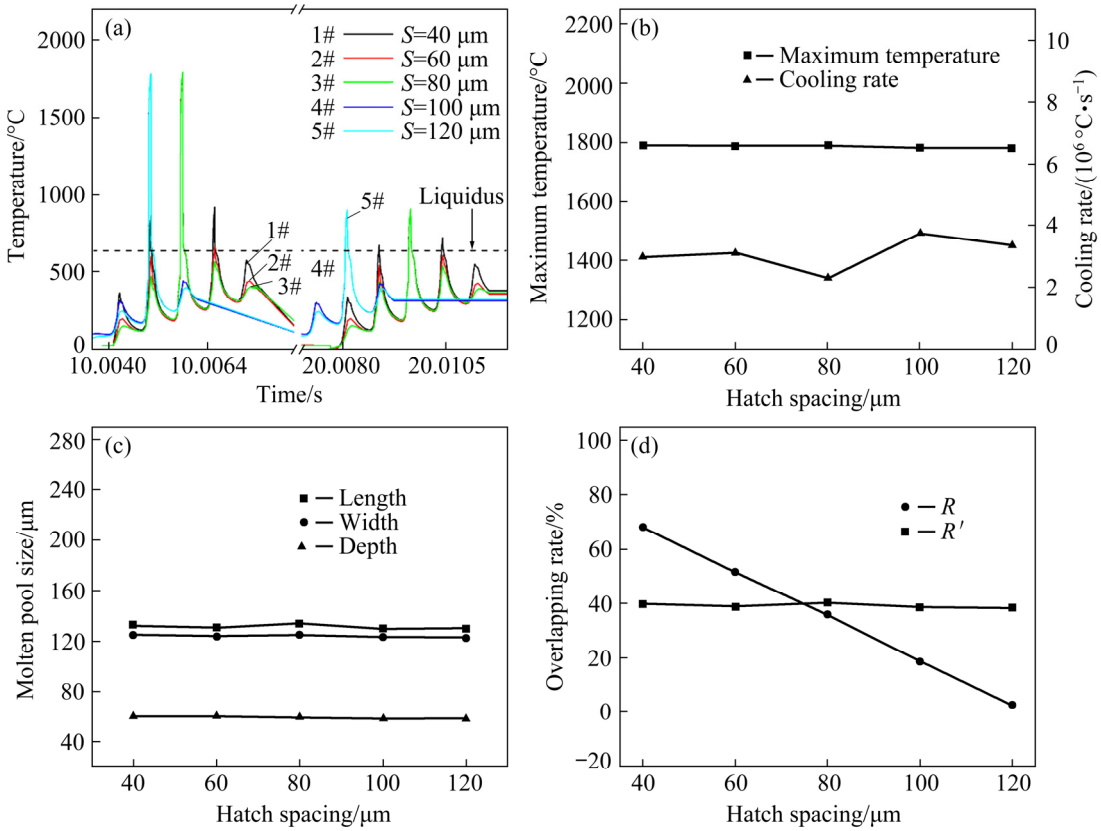

Fig. 7 Temperature−time curves (a), maximum temperature and cooling rate (b), molten pool size (c), and overlapping rate (d) at P2 with different hatch spacings under laser power of 350 W and point distance of 80 μm

under laser power 350 W, point distance 80 μm and hatch spacing 80 μm were analyzed, and the results are shown in Fig. 8. As can be seen in Figs. 8(a,b), the maximum equivalent stress on the formed solid increases from 209 to 238 MPa as the laser beam moves from the middle to the end of the first track. It can also be found that there is no thermal stress in the liquid molten pool and the maximum equivalent stress is located at the junction of the formed solid and the powders, where the alloy cooled sufficiently and is more susceptible to shrinkage. When the laser beam moves to the end of the second track in the opposite direction, the equivalent stress of the formed solid of the first track near the molten pool decreases due to heat transfer from the heat source. The highest equivalent stress is located at the end of the first track (Fig. 8(c)).

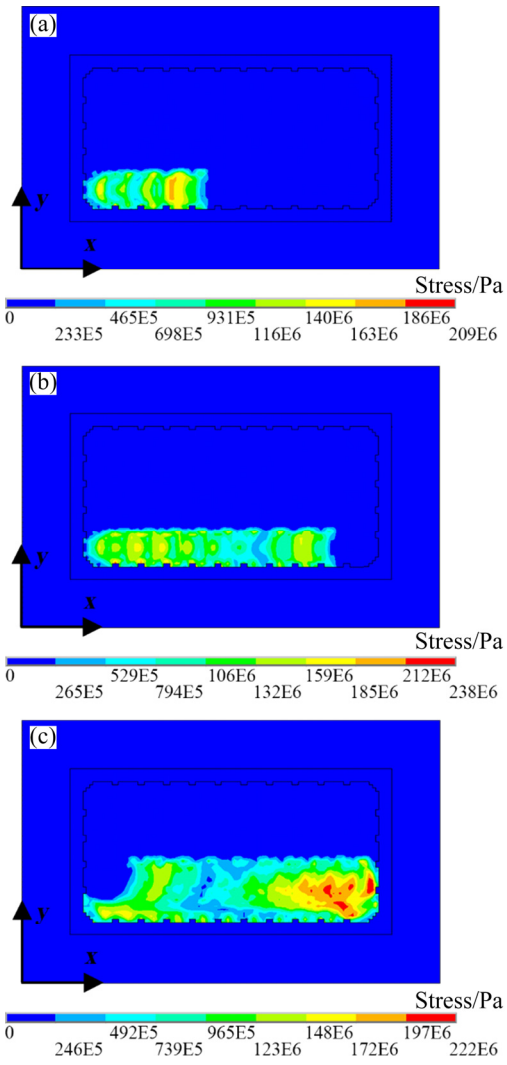

Fig. 8 Equivalent stress diagram at different time under laser power of 350 W, point distance of 80 μm and hatch spacing of 80 μm: (a) t=420 μs; (b) t=770 μs; (c) t=1540 μs

When the powder bed cools down to room temperature, high residual stresses are inevitably present in the formed alloy due to dimensional shrinkage [31], and excessive residual stresses can affect the mechanical properties of the alloy. Figure 9 depicts the residual stress distribution in varying directions when the model cools down to room temperature with laser power 350 W, point distance 80 μm and hatch spacing 80 μm. Obviously, the residual stresses in the alloy are mainly tensile stresses (the stress value is positive), and they are always higher than the compressive stresses. It is also noted that the maximum tensile stress is mainly distributed in the scanning direction with a maximum value of 358 MPa, which would result in microcracks being more likely to form and propagate along the direction perpendicular to the scanning direction. This is consistent with the results reported in most of the literature. On the contrary, the tensile stresses in the y- and z-directions are mainly concentrated at the edges of the formed alloy (Figs. 9(b, c)), which is the main reason for the warping of the formed parts.

4.2.2 Residual stress with different process parameters

Figure 10 shows the equivalent residual stress distribution along the x-direction on the first track at different process parameters. It can be seen that the residual stresses are concentrated in the middle of the scanning track and show periodic fluctuations. For each molten pool, the highest residual stress is located in the overlapping area, where the alloy is most constrained by the formed alloy. Away from the overlapping area, the alloy is less constrained by the formed alloy and therefore it has a low residual stress. This difference of the residual stress in different parts of the molten pool is responsible for the periodic fluctuations. As can be seen in Fig. 10(a), as the laser power increases, the fluctuation amplitude of the stress gradually decreases. This is mainly due to the fact that the higher the laser power, the larger the molten pool size and the smaller the temperature gradients in different parts of the molten pool. When the point distance is lower than 130 μm, as the point distance increases, the maximum residual stress gradually increases and the minimum residual stress gradually decreases (Fig. 10(b)). This is consistent with the results reported by WANG et al [32]. When the point distance is 130 μm, the low overlapping rate

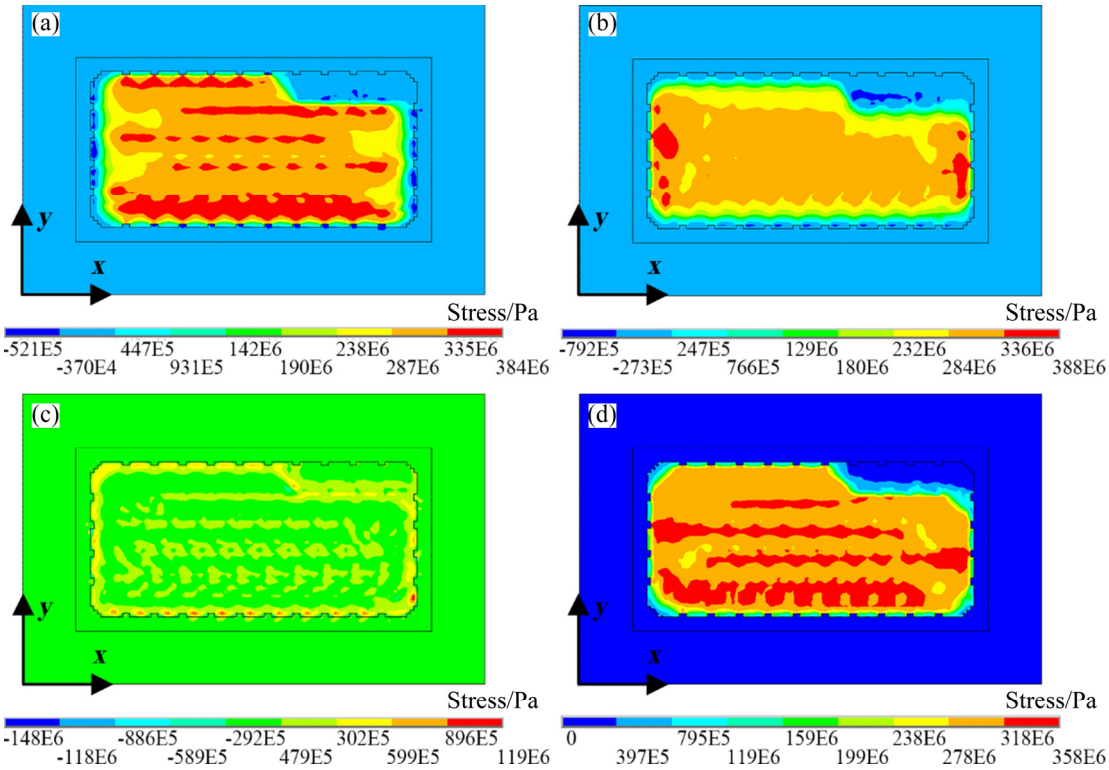

Fig. 9 Residual stress distributions with whole model cooling down to room temperature under laser power of 350 W, point distance of 80 μm and hatch spacing of 80 μm: (a) *x*-component of stress; (b) *y*-component of stress; (c) *z*-component of stress; (d) von Mises stress

results in unmelted powders along the *x*-axis, which leads to a significant reduction of the residual stress. It can also be seen in Fig. 10(c) that as the hatch spacing increases, the residual stress does not change much. Based on the previous temperature field analysis, the hatch spacing has little effect on the maximum temperature and cooling rate, and therefore its effect on the stress field is also small.

4.3 Experimental investigation and simulation validation

Figure 11 shows the relative density and hardness of the samples under different laser powers. As the laser power increases, the density of the alloy increases and then decreases. When the laser power is 375 W, the highest density of 99.5% is obtained. In addition, the hardness of the selective laser melted Al−Mg−Sc−Zr alloy decreases from HB 114.2 to HB 104.5 with increasing laser power. The hardness depends not only on the density, but also on the crystal structure, grain size and supersaturation of the alloy. The higher the density of the alloy, the smaller the grain size, and the higher the hardness of the alloy. Based on the previous simulation results, it is known that the higher the laser power, the longer the liquid lifetime of the molten pool. On one hand, excessively long liquid lifetime causes Mg to precipitate more easily from the Al matrix, weakening the solid solution strengthening effect. On the other hand, too long liquid lifetime causes the alloy grains to grow up more easily, thus weakening the grain strengthening effect. Therefore, as the laser power increases, the hardness value of the alloy decreases. Considering the relative density and hardness, the optimal laser power ranges from 325 to 375 W.

Metallographic photographs of the *x*−*z* surface of the selective laser melted Al−Mg−Sc−Zr samples under different laser powers are shown in Fig. 12. The fish molten pool is composed of columnar grain regions (bright regions) and fine equiaxed grain regions (dark regions). Details on the alloy microstructure were reported in Refs. [13,26]. This is obviously different from the microstructure of traditional as-cast samples. Selective laser melted AlSi10Mg alloy [14], Inconel 718 alloy [33,34] and Ti−6Al−7Nb alloy [35] also have similar

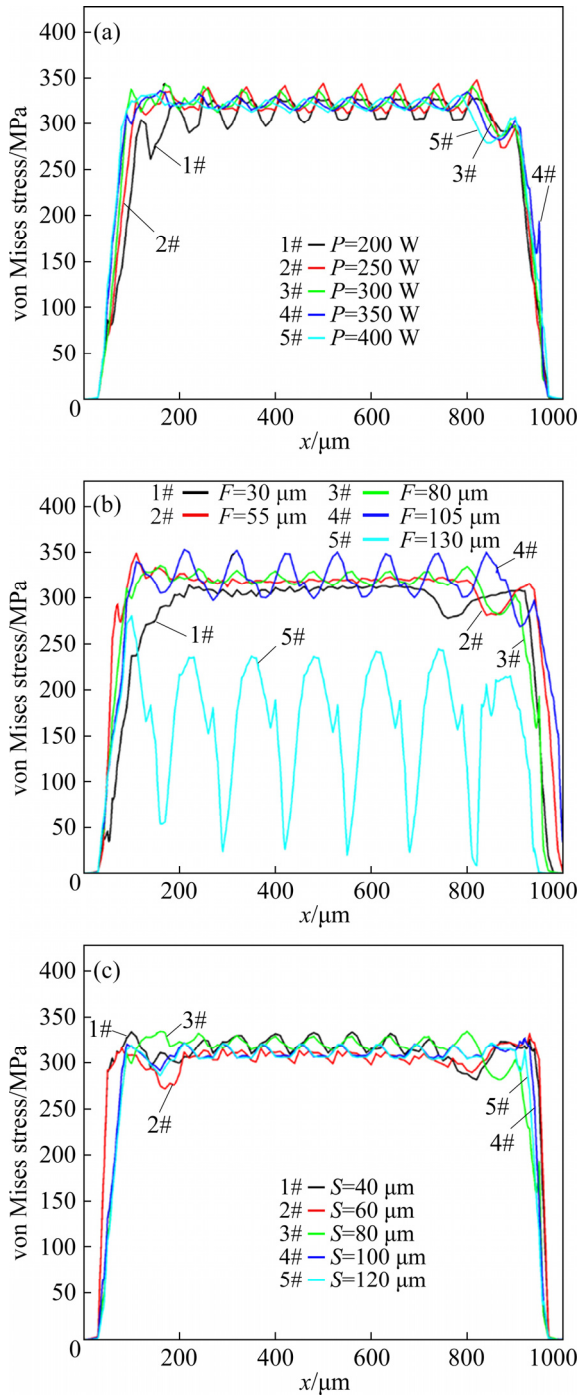

Fig. 10 Residual stress distribution along *x*-direction on first track at different laser powers (a), point distances (b) and hatch spacings (c)

microstructure. It can also be seen that there are obvious differences in the geometric size of the molten pool under different powers. The higher the laser power, the larger the molten pool size.

In order to verify the accuracy of the simulation results, the molten pool sizes under different parameters were measured based on the

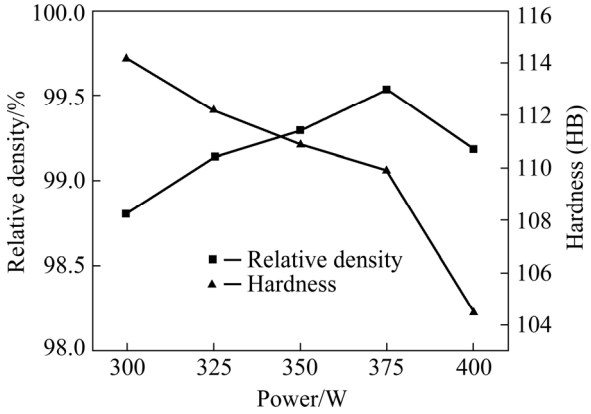

Fig. 11 Relative density and hardness of samples under different laser powers

molten pools on the top layer of the metallographic photographs referring to Ref. [36], and the results are shown in Fig. 13. As can be seen, simulation results have a good agreement with the experimental data. The main reasons for the error in the experimental results and simultaneous data are as follows.

(1) The FEM simulation ignores the effects of the recoil pressure generated by the evaporation on the heat transfer in the molten pool.

(2) The physical property parameters used in the simulation are different from the actual values.

(3) The finite element model for three layers and five tracks is too small to fully simulate the actual situation.

(4) The molten pool sizes at different positions in the alloy are different, and there is a certain error in the actual measurement process.

Figure 14 shows the relative density and hardness of the samples under different point distances and hatch spacings. As can be seen, with the increase of the point distance and hatch spacing, the relative density of the alloy increases and then decreases. This phenomenon is related to the overlapping rate, which has been discussed in above sections. As the point distance increases, the hardness of the alloy increases and then decreases. The maximum hardness value of HB 114.2 is obtained at a point distance of 60 μm. The hardness of the alloy is the combined effect of the density and the strengthening effect. As the hatch spacing increases, the hardness of the sample is in the range of HB 109−111. According to the above analysis, the hatch spacing has little effect on the temperature field of the molten pool, so the

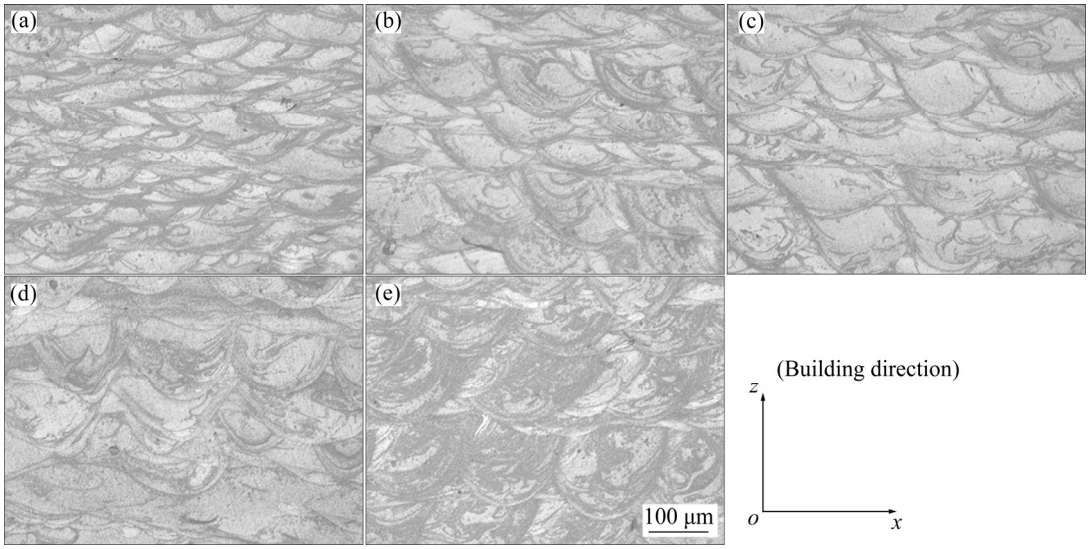

Fig. 12 Metallographic photographs of x−z surface of selective laser melted samples under different laser powers: (a) 300 W; (b) 325 W; (c) 350 W; (d) 375 W; (e) 400 W

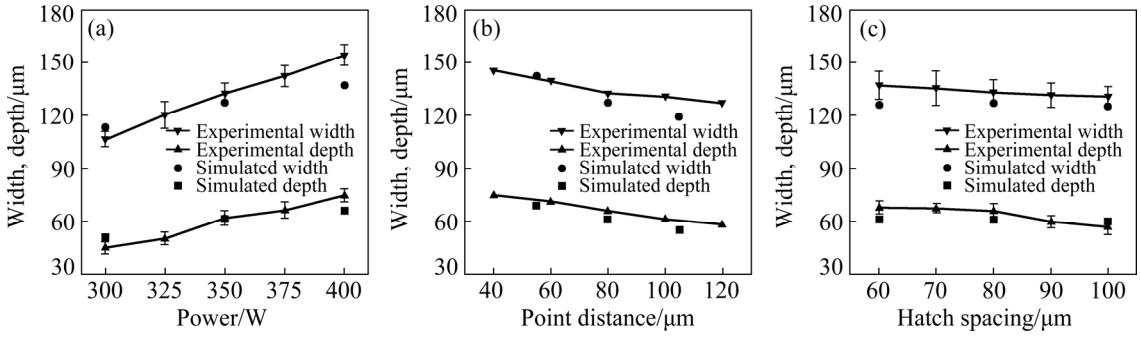

Fig. 13 Molten pool sizes of selective laser melted Al−Mg−Sc−Zr alloy under different powers (a), point distances (b) and hatch spacings (c)

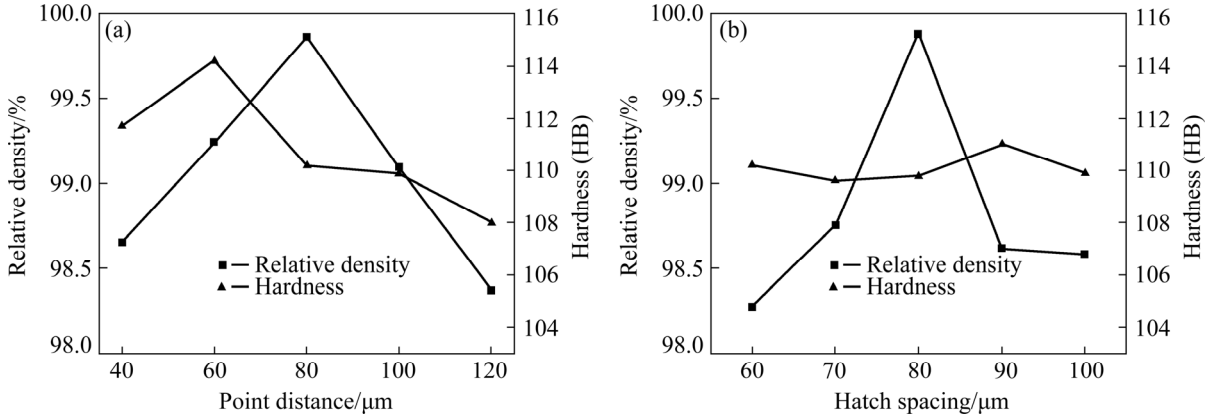

Fig. 14 Relative density and hardness of samples under different point distances (a) and hatch spacings (b)

microstructure of the alloy is similar and the hardness does not very much. Considering the relative density and hardness, the optimal point distance and hatch spacing are 80−100 μm and 80 μm, respectively.

In order to evaluate the combined effects of the process parameters, the volume energy density (VED) is defined as

$$\mathrm{VED}=\frac{Pt_{\mathrm{E}}}{FdS} \tag{22}$$

Volume energy density can provide the key method and scientific mechanism for the control of microstructure, metallurgical defects and properties

of selective laser melted alloy [37].

Figure 15 shows the relationship between the volumetric energy density and the relative density of the Al−Mg−Sc−Zr alloy. When the hatch spacing is 90 and 100 μm (within the dashed black line), the low overlapping rate between adjacent scanning tracks severely damage the stable state of the selective laser melting, so the relative density of the alloy mainly depends on the factors that destabilize the forming process. After discarding the destabilization data, it can be found that as the volumetric energy density increases, the relative density of the alloy tends to increase and then decrease. Both too low and too high volumetric energy densities can lead to an increase in defects in the samples and a decrease in the density. When the volumetric energy density is in the range of 100−160 J/mm^3, the high relative density (>99%) of the samples is conducive to obtaining high quality alloy parts.

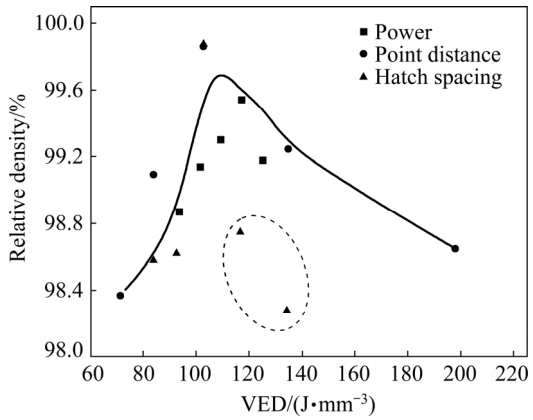

Fig. 15 Relationship between volume energy density and relative density

By considering the density and hardness of the samples, the optimized process parameters for selective laser melted Al−Mg−Sc−Zr alloy are laser power of 325−375 W, point distance of 80−100 μm, hatch spacing of 80 μm, and volume energy density of 100−160 J/mm^3. Details on the microstructure and mechanical properties of the selective laser melted Al−Mg−Sc−Zr alloy under the optimized parameters were reported in Ref. [26].

5 Conclusions

(1) The maximum temperature, molten pool size, and overlapping rate increase approximately linearly as the laser power increases from 200 to 400 W. An opposite trend is observed as the point distance increases from 30 to 130 μm. As the hatch spacing increases from 40 to 120 μm, the maximum temperature and the molten pool size remain essentially unchanged, but the overlapping rate between the adjacent tracks drops sharply.

(2) When the powder bed cools down to room temperature, the residual stresses are mainly tensile stress with the *x*-component being the highest. The residual stresses tend to concentrate in the first scanning track and the beginning and end of each scanning track.

(3) As the volume energy density increases (laser power increases, point distance and hatch spacing decrease), the relative density of the samples tends to increase and then decrease. The optimized process parameters are laser power 325−375 W, point distance 80−100 μm and hatch spacing 80 μm. The relative density of the alloy are >99% under the optimized process conditions.

Acknowledgments

The authors are grateful for the financial supports from the National Natural Science Foundation of China (No. 51804349), the China Postdoctoral Science Foundation (No. 2018M632986), the Natural Science Foundation of Hunan Province, China (No. 2019JJ50766), and the National Key Laboratory of Science and Technology on High-strength Structural Materials, China (No. JCKY201851).

References

[1] THIJS L, VERHAEGHE F, CRAEGHS T, van HUMBEECK J, KRUTH J P. A study of the micro structural evolution during selective laser melting of Ti−6Al−4V [J]. Acta Materialia, 2010, 58(9): 3303−3312.

[2] AZIZI H, ZUROB H, BOSE B, GHIAASIAAN S R, WANG X, COULSON S, DUZ V, PHILLION A B. Additive manufacturing of a novel Ti−Al−V−Fe alloy using selective laser melting [J]. Additive Manufacturing, 2018, 21: 529−535.

[3] BARTOLOMEU F, BUCIUMEANU M, ALVES N, SILVA F, CARVALHO O, MIRANDA G. Wear behavior of Ti6Al4V biomedical alloys processed by selective laser melting, hot pressing and conventional casting [J]. Transactions of Nonferrous Metals Society of China, 2017, 27: 829−838.

[4] GUAN K, WANG Z M, GAO M, LI X Y, ZENG X Y. Effects of processing parameters on tensile properties of selective laser melted 304 stainless steel [J]. Materials & Design, 2013, 50(17): 581−586.

[5] KURNSTEINER P, WILMS M B, WEISHEIT A, BARRIOBERO-VILA P, JAGLE E A, RAABE D. Massive nanoprecipitation in an Fe−19Ni−*x*Al maraging steel triggered by the intrinsic heat treatment during laser metal deposition [J]. Acta Materialia, 2017, 129: 52−60.

[6] LARRÁYOZ IZCARA X, GUIRAO BLANK A, PYCZAK F, STARON P, SCHUMANN S, HUBER N. Characterization and modeling of the influence of artificial aging on the microstructural evolution of age-hardenable AlSi10Mg(Cu) aluminum alloys [J]. Materials Science and Engineering A, 2014, 610: 46−53.

[7] WANG L F, SUN J, YU X L, SHI Y, ZHU X G, CHENG L Y, LIANG H H, YAN B, GUO L J. Enhancement in mechanical properties of selectively laser-melted AlSi10Mg aluminum alloys by T6-like heat treatment [J]. Materials Science and Engineering A, 2018, 734: 299−310.

[8] WANG P, ECKERT J, PRASHANTH K G, WU M W, SCUDINO S. A review of particulate-reinforced aluminum matrix composites fabricated by selective laser melting [J]. Transactions of Nonferrous Metals Society of China, 2020, 30: 2001−2034.

[9] GLODE S, KLEMENC J, ZUPANI F, VESENJAK M. High-cycle fatigue and fracture behaviours of SLM AlSi10Mg alloy [J]. Transactions of Nonferrous Metals Society of China, 2020, 30(10): 2577−2589.

[10] SPIERINGS A B, DAWSON K, VOEGTLIN M, PALM F, UGGOWITZER P J. Microstructure and mechanical properties of as-processed scandium-modified aluminium using selective laser melting [J]. CIRP Annals, 2016, 65(1): 213−216.

[11] SPIERINGS A B, DAWSON K, KERN K, PALM F, WEGENER K. SLM-processed Sc- and Zr- modified Al−Mg alloy: Mechanical properties and microstructural effects of heat treatment [J]. Materials Science and Engineering A, 2017, 701: 264−273.

[12] ZHANG H, GU D D, YANG J K, DAI D H, ZHAO T, HONG C, GASSER A, POPRAWE R. Selective laser melting of rare earth element Sc modified aluminum alloy: Thermodynamics of precipitation behavior and its influence on mechanical properties [J]. Additive Manufacturing, 2018, 23: 1−12.

[13] MA R L, PENG C Q, CAI Z Y, WANG R C, ZHOU Z H, LI X G, CAO X Y. Manipulating the microstructure and tensile properties of selective laser melted Al−Mg−Sc−Zr alloy through heat treatment [J]. Journal of Alloys and Compounds, 2020, 831: 154773.

[14] ZHOU L, MEHTA A, SCHULZ E, McWILLIAMS B, CHO K, SOHN Y. Microstructure, precipitates and hardness of selectively laser melted AlSi10Mg alloy before and after heat treatment [J]. Materials Characterization, 2018, 143: 5−17.

[15] CHEN H, WEI Q S, ZHANG Y J, CHEN F, SHI Y S, YAN W T. Powder-spreading mechanisms in powder-bed-based additive manufacturing: Experiments and computational modeling [J]. Acta Materialia, 2019, 179: 158−171.

[16] CHEN H, CHEN Y X, LIU Y, WEI Q S, SHI Y S, YAN W T. Packing quality of powder layer during counter-rolling-type powder spreading process in additive manufacturing [J]. International Journal of Machine Tools and Manufacture, 2020, 153: 103553.

[17] ILIN A, LOGVINOV R, KULIKOV A, PRIHODOVSKY A, XU H, PLOSHIKHIN V, GÜNTHER B, BECHMANN F. Computer aided optimisation of the thermal management during laser beam melting process [J]. Physics Procedia, 2014, 56: 390−399.

[18] WEINGARTEN C, BUCHBINDER D, PIRCH N, MEINERS W, WISSENBACH K, POPRAWE R. Formation and reduction of hydrogen porosity during selective laser melting of AlSi10Mg [J]. Journal of Materials Processing Technology, 2015, 221: 112−120.

[19] LUO C, QIU J, YAN Y, YANG J, UHER C, TANG X. Finite element analysis of temperature and stress fields during the selective laser melting process of thermoelectric SnTe [J]. Journal of Materials Processing Technology, 2018, 261: 74−85.

[20] LI Biao-qiang. Selective laser melting of AlSi10Mg: Simulation and experiments [D]. Taiyuan: North University of China, 2019. (in Chinese)

[21] SONG B, DONG S J, LIAO H L, CODDET C. Process parameter selection for selective laser melting of Ti6Al4V based on temperature distribution simulation and experimental sintering [J]. The International Journal of Advanced Manufacturing Technology, 2012, 61(9): 967−974.

[22] LI M Y, HAN Y C, ZHOU M Y, CHEN P, GAO H, ZHANG Y, ZHOU H M. Experimental investigating and numerical simulations of the thermal behavior and process optimization for selective laser sintering of PA6 [J]. Journal of Manufacturing Processes, 2020, 56: 271−279.

[23] BEIRANVAND Z M, GHAINI F M, MOOSAVY H N, SHEIKHI M, TORKAMANY M J, MORADI M. The relation between magnesium evaporation and laser absorption and weld penetration in pulsed laser welding of aluminum alloys: Experimental and numerical investigations [J]. Optics & Laser Technology, 2020, 128: 106170.

[24] MAJEED M, VURAL M, RAJA S, BILAL NAIM SHAIKH M. Finite element analysis of thermal behavior in maraging steel during SLM process [J]. Optik, 2020, 208: 164128.

[25] HUSSEIN A, HAO L, YAN C, EVERSON R. Finite element simulation of the temperature and stress fields in single layers built without-support in selective laser melting [J]. Materials & Design, 2013, 52: 638−647.

[26] MA R L, PENG C Q, CAI Z Y, WANG R C, ZHOU Z H, LI X G, CAO X Y. Effect of bimodal microstructure on the tensile properties of selective laser melt Al−Mg−Sc−Zr alloy [J]. Journal of Alloys and Compounds, 2019, 815: 152422.

[27] XU G, LUO K Y, DAI F Z, LU J Z. Effects of scanning path and overlapping rate on residual stress of 316L stainless steel blade subjected to massive laser shock peening treatment with square spots [J]. Applied Surface Science, 2019, 481: 1053−1063.

[28] CHEN C, YIN J, ZHU H, XIAO Z, ZHANG L, ZENG X. Effect of overlap rate and pattern on residual stress in selective laser melting [J]. International Journal of Machine Tools and Manufacture, 2019, 145: 103433.

[29] CAO J, LIU F C, LIN X, HUANG C P, CHEN J, HUANG W D. Effect of overlap rate on recrystallization behaviors of Laser Solid Formed Inconel 718 superalloy [J]. Optics & Laser Technology, 2013, 45: 228−235.

[30] LI Y L, GU D D. Parametric analysis of thermal behavior during selective laser melting additive manufacturing of aluminum alloy powder [J]. Materials & Design, 2014, 63(2): 856−867.
[31] ABOULKHAIR N T, MASKERY I, TUCK C, ASHCROFT I, EVERITT N M. On the formation of A1Si10Mg single tracks and layers in selective laser melting: Microstructure and nano-mechanical properties [J]. Journal of Materials Processing Technology, 2016, 230: 88−98.
[32] WANG Lian-feng, JIANG Xiao-hui, ZHU Yi-hong, ZHU Xiao-gang, SUN Jing, YAN Biao. An approach to predict the residual stress and distortion during the selective laser melting of AlSi10Mg parts [J]. International Journal of Advanced Manufacturing Technology, 2018, 97: 1−12.
[33] LI X, SHI J J, WANG C H, CAO G H, RUSSELL A M, ZHOU Z J, LI C P, CHEN G F. Effect of heat treatment on microstructure evolution of Inconel 718 alloy fabricated by selective laser melting [J]. Journal of Alloys and Compounds, 2018, 764: 639−649.
[34] TUCHO W M, CUVILLIER P, SJOLYST-KVEMELAND A, HANSEN V. Microstructure and hardness studies of Inconel 718 manufactured by selective laser melting before and after solution heat treatment [J]. Materials Science and Engineering A, 2017, 689: 220−232.
[35] CHLEBUS E, KUZNICKA B, KURZYNOWSKI T, DYBALA B. Microstructure and mechanical behaviour of Ti−6Al−7Nb alloy produced by selective laser melting [J]. Materials Characterization, 2011, 62(5): 488−495.
[36] KIM T, HA K, CHO Y R, JEON J B, LEE W. Analysis of residual stress evolution during powder bed fusionprocess of AISI 316L stainless steel with experiment and numerical modeling [J]. The International Journal of Advanced Manufacturing Technology, 2019, 105(5−8): 1−15.
[37] GU D D, MEINERS W, WISSENBACH K, POPRAWE R. Laser additive manufacturing of metallic components: materials, processes and mechanisms [J]. International Materials Reviews, 2012, 57(3): 133−164.

选区激光熔化 Al−Mg−Sc−Zr 合金温度场和应力场有限元模拟

马如龙[1]，彭超群[1]，蔡志勇[1,2]，王日初[1,2]，周朝辉[3]，李晓庚[3]，曹玄扬[3]

1. 中南大学 材料科学与工程学院，长沙 410083；
2. 中南大学 轻质高强结构材料重点实验室，长沙 410083；
3. 长沙新材料产业研究院有限公司，长沙 410083

摘 要：为研究选区激光熔化 Al−Mg−Sc−Zr 合金的温度场和应力场，建立三维有限元分析模型。在考虑粉末−固体转变、材料热物理性能参数随温度变化、相变潜热和熔池对流的基础上，研究激光功率、点间距和扫描间距对温度场分布、熔池尺寸和残余应力场分布的影响。然后，采用实验法探讨激光功率、点间距和扫描间距对合金组织、相对密度和硬度的影响。结果表明：随着激光功率增大、点间距减小和扫描间距的减小，熔池尺寸逐渐增大。残余应力主要分布在第一个扫描道次的中间以及每一个扫描道次的起点和终点。实验结果证明有限元模拟的有效性。随着激光功率增大、点间距减小和扫描间距减小，试样的致密度先增大后减小。试样的最佳工艺参数区间为激光功率 325~375 W、点间距 80~100 μm 和扫描间距 80 μm。

关键词：Al−Mg 合金；Al−Mg−Sc−Zr 合金；选区激光熔化；有限元分析；温度场；应力场

(Edited by Xiang-qun LI)